T.1: Development of FBG sensors and their validation for field deployment in high EMI, nuclear radiation, chemical and industrial environment

O. Prakash[*,1,3], **J. Kumar**[1], **R. Mahakud**[1], **P. K. Saini**[1,3], **M. K. Saxena**[1], **S. K. Dixit**[1,3], **S. V. Nakhe**[2]
[1]*Fiber Sensors& Optical Spectroscopy Section*
[2]*Laser Group*
[3]*Homi Bhabha National Institute, Mumbai*
[*]*Email: oprakash@rrcat.gov.in*

Abstract

Different types of fiber Bragg grating (FBG) such as Type-I, Type-IIa, tilted and regenerated, are fabricated using the in-house developed high repetition rate (~5.5 kHz), high quality ultraviolet (UV) (255 nm) beam. These FBGs have been used in development of customized single point/multipoint temperature sensors, strain sensor and refractive index sensor for their operation in high electromagnetic interference (EMI) and radiation environment. A novel concept of only amplitude dependent refractive index sensing using regenerated FBG is also presented.

1. Introduction

The conventional temperature or strain sensors are likely to malfunction, transform or drift in high EMI, nuclear radiation and chemical environment [1-2]. In such situations, fiber optic sensors provide an alternative approach for measurement of different parameters, including temperature, strain, pressure, vibrations, force etc. [3-4]. FBG represents a periodic modulation of the refractive index (RI) in a fiber core over a fixed length. The RI modulation of submicron period is imprinted in the photosensitive fiber core by exposing it to the CW/ns pulses of UV interference pattern, or by fs pulses (IR and UV) in non-photosensitive fiber. The pitch, strength of RI modulation and grating length decide the spectral and reflection/transmission characteristics of a FBG.The advantages of FBG sensor over competing technologies are high spatial resolution, single point as well as distributed sensing capabilities, high sensitivity, fast response time, accessibility to difficult and remote locations and capability to work in harsh environment such as high EMI and radiation field [5]. In the present theme article, inscription of different types of FBGs using indigenously developed high repetition rate (~5.5 kHz), highly coherent UV radiation at 255 nm is presented. The article presents design, development and deployment of FBG based sensors for temperature sensing in acidic, high radiation and high EMI environments. The article also discusses the development and deployment of strain and refractive index sensors.

2. Resonant mode coupling in fiber Bragg gratings

In FBG, the coupling takes place between two counter propagating identical modes i.e. forward propagating core mode to backward propagating core mode, as shown in Figure T.1.1. The resonant Bragg wavelength is given by,

$$\lambda_B = 2n_{co,eff}\Lambda \tag{1}$$

Where $n_{co,eff}$ is the effective refractive index of core mode and Λ is the period of the FBG

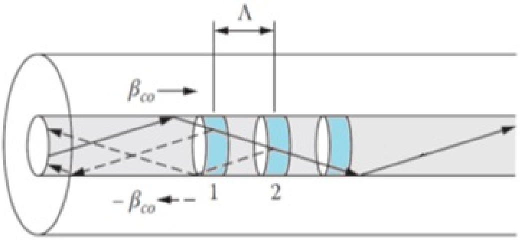

Fig. T.1.1: Light coupling between forward and backward propagating core mode in FBG.

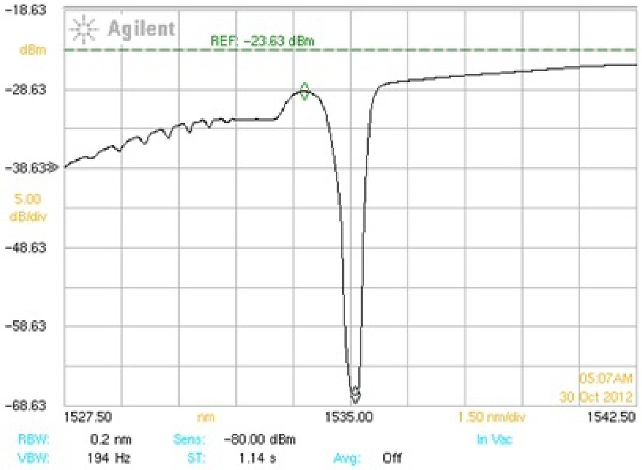

Fig. T.1.2: Transmission spectrum of FBG.

For uniform grating, the reflectivity of the FBG is given by [6]

$$R=\tanh^2(\kappa L) \tag{2}$$

The coupling coefficient, κ, for the sinusoidal variation of index perturbation along the fiber axis is given by

$$\kappa = \frac{\pi\,\Delta n\,\eta}{\lambda}, \tag{3}$$

where Δn is change in the refractive index, $\eta=1-1/V^2$, $V\geq2.4$, and is a function of the fiber parameter V, which represents the fraction of the integrated fundamental-mode intensity contained in the core. Figure T.1.2 shows the typical transmission spectrum of FBG fabricated at RRCAT. The reflectivity of the fiber Bragg grating is calculated from the observed transmission dip (T_d in dB), given as[7]

$$R=1-10^{-Td/10} \tag{4}$$

3. Development of FBG writing set-up

In RRCAT, a FBG inscription set-up is developed using high repetition rate, low peak power, highly coherent 255 nm radiation. Figure T.1.3 shows the combined experimental setup for the second harmonic (SH) generation of copper vapour laser (CVL) and FBG fabrication using phase-mask [7]. Highly coherent UV laser beam (λ ~255 nm) is generated from the SH conversion of CVL [8,9]. Finally, UV beam interference pattern of submicron period is created by either phase-mask, as shown in Figure T.1.3 or by bi-prism [10].

The experimental set-up for FBG writing using bi-prism was similar to Figure T.1.3, except phase-mask is replaced by the bi-prism. The apex angle of used bi-prism was 24° for C-band FBG at 1550 nm [11].

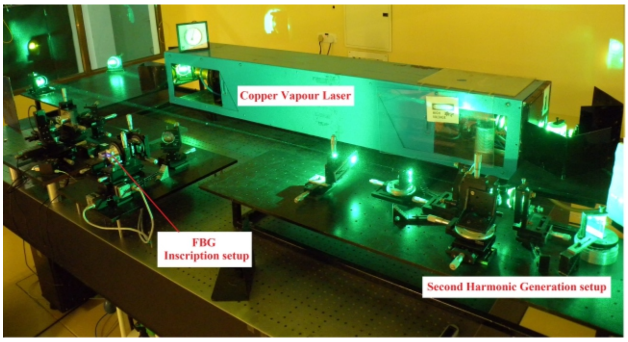

Fig. T.1.3: Experimental set-up for phase-mask based FBG writing set-up using 255 nm beam.

4. Experimental results on inscription of different types of FBGs

4.1 Inscription of Type-I FBG

Type-I FBG is characterized by the monotonous growth of refractive index modulation with UV fluence. The FBGs of length ~10 mm are written in non-hydrogenated photosensitive SM-1500 fused silica fiber (doping: typical Ge ~ 18 mol %, Fiber Core), with 255 nm UV using phase mask. Figure T.1.4 shows the variation in RI modulation and reflectivity at different fluences.

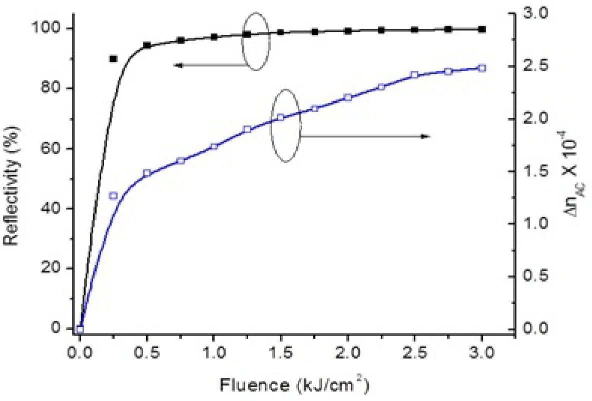

Fig. T.1.4: Variation of RI modulation and reflectivity with fluence for Type-I FBG

The refractive index modulation (Δn_{ac}) is estimated from the reflectivity of the FBG, grating length L and Bragg wavelength λ_B, using the relation [6, 12]

$$\Delta n_{ac} = \frac{\lambda_B}{\pi \eta L} \tanh^{-1}\left(\sqrt{R}\right). \qquad (5)$$

The average refractive index change (Δn_{dc}) is estimated from the Bragg wavelength shift $\Delta\lambda_B$ during writing FBG [6, 12],

$$\Delta n_{dc} = \frac{\Delta\lambda_B n_{eff}}{\eta \lambda_B}, \qquad (6)$$

where η is mode overlap integral. For typical fibers used, the parameter η is about 0.85. The estimated refractive index modulation (Δn_{ac}) was 2.5×10^{-4} at 3.09 kJ/cm^2. For accumulated fluence of 3.09 kJ/cm^2, the average refractive index change reaches to value of 3.25×10^{-4}.

4.2 Fabrication of Type-IIa FBGs

Type-IIa or negative refractive index grating are observed due to regrowth of the refractive index modulation subsequent to decay of Type-I FBG with prolonged UV exposure [13]. After attaining the maximum value, the refractive index modulation starts to decrease (full or partial erasure of Type-I grating) and also the wavelength shifts back to shorter wavelength (blue shifted) or remains constant [13]. Figure T.1.5 shows the reflectivity, refractive index modulation (Δn_{ac}), and average refractive index change (Δn_{dc}) for Type IIa grating. From the Figure T.1.5, it is noticed that the reflectivity and refractive index modulation (Δn_{ac}) increases with the UV fluence and reaches the maximum value of 99% and 1.63×10^{-4} respectively, at the cumulative fluence of 5.76 kJ/cm^2. As the fluence is increased further, the reflectivity and index modulation reduced to 2.3% and 0.08×10^{-4} respectively at the fluence of 24.45 kJ/cm^2. Thereafter, reflectivity and refractive index modulation again increases and ultimately reaches to 40 % and 0.42×10^{-4}, respectively, at the fluence of 37.4 kJ/cm^2. It has been observed that the refractive index rollover depends on the doping concentration of photosensitive fibers [14].

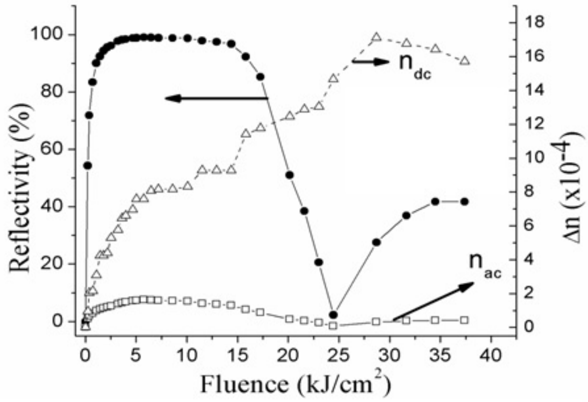

Fig. T.1.5: Variation of reflectivity, index modulation and dc refractive index change for Type-IIa FBG.

4.3 Inscription of thermally regenerated grating in hydrogenated fiber

The regenerated fiber Bragg gratings (RFBGs) can be obtained through high temperature annealing treatment of Type-I seed FBGs written in hydrogenated fiber [15]. Hydrogen loading at ~100 bar pressure is carried for about 144 hours, keeping the temperature constant at ~100 °C in an in-house developed H_2 loading set-up at RRCAT [16]. The seed Type-I FBG of transmission dip ~40 dB (reflectivity ~ 99.99%) is written in hydrogen loaded SMF-28 fiber. The ramp annealing schedule is applied along the FBG for regeneration. At 900 ^{0}C, the grating erased almost completely within 25 minutes and then regeneration started. The maximum reflectivity of regenerated grating ~ 88% (~ 8.8 dB) is observed in about 130 minutes.

4.4 Inscription of tilted fiber Bragg grating

In a uniform FBG, the grating planes are normal to fiber axis. However, the Bragg resonant wavelength of a FBG can be tuned in a limited range by tilting the fiber in the fringe plane as shown in Figure T.1.6 [17].

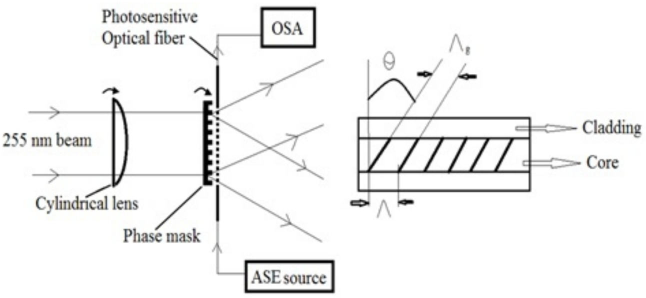

Fig.T.1.6: Experimental set-up for writing tilted fiber Bragg grating.

The induced index planes in the core of the fiber will be tilted at angle θ with normal. The tilt angle can be introduced by rotating the phase-mask and cylindrical lens in the vertical plane by same angle so that the line focus remains on the fiber. For the tilted grating, the resonance condition for the core mode can be written as

$$\lambda_{Bragg} = \left(n_{co,eff} + n_{co,eff}\right)\Lambda \tag{8}$$

The resonance wavelengths of the cladding modes are given by:

$$\lambda_{Bragg} = \left(n_{co,eff} + n_{eff,cl,i}\right)\frac{\Lambda_g}{\cos\theta} \tag{9}$$

where θ is the angle between grating fringe and the fiber cross-section, $n_{eff,cl,i}$ is the effective refractive index of i^{th} cladding mode and Λ_g is grating period along the tilt. Figure T.1.7 shows the typical transmission spectra for grating tilt angle of 3° [17]. It is observed that at 3° tilt angle, the main Bragg peak shifted towards the higher wavelength compared to tilt angle of 0° and also transmission dip is decreased. However, the transmission dip of the cladding modes is increased.

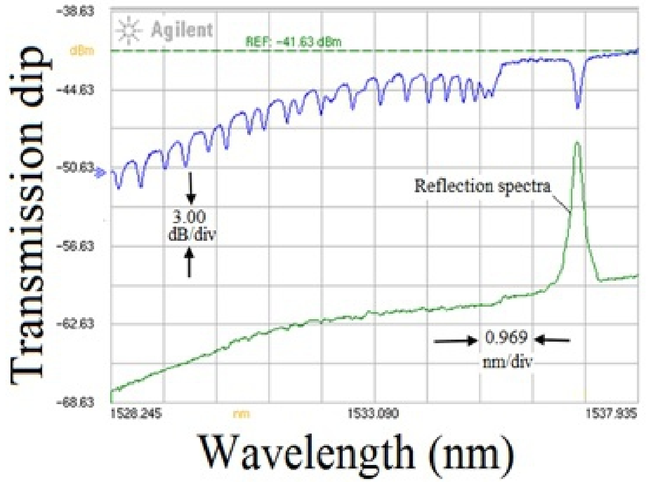

Fig. T.1.7: Transmission (upper trace) and refection spectra (lower trace) for grating tilt angle 3°.

4.5 Inscription of multiple FBGs in a single fiber

The phase matching condition for the Bragg reflection wavelength λ_{Bragg} of a tilted FBG (TFBG) for the core mode can be expressed as follows:

$$\lambda_{Bragg} = \frac{2n_{co,eff}\Lambda}{\cos\theta}, \tag{10}$$

where θ is the tilt angle, $n_{co,eff}$ is the effective refractive index of the core mode and Λ corresponds to the normal grating period. The Bragg wavelength can be changed either by changing the phase-mask period or tilt angle or both. However, the tilt angle can be increased to only certain extent since the coupling coefficient decreases with increase in tilt angle. The Bragg wavelength can be also tuned by diverging/converging UV beam and single bi-prism [18]. Figure T.1.8 shows the typical reflection spectra of 20 FBGs written in single fiber by tilting the phase-mask and changing the mask period.

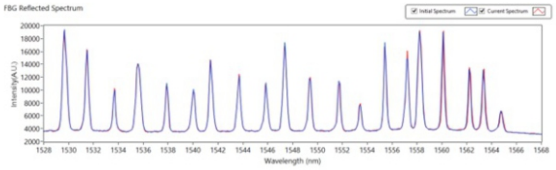

Fig. T.1.8: Bragg wavelength of 20 FBGs written by changing the phase mask period and tilt angle.

5. Development of FBGs based sensors

5.1 Single point and multipoint temperature sensors

The Bragg wavelength shift with temperature is given by [19]:

$$\lambda_B = \frac{d\lambda_B}{dT}\Delta T = \lambda_B\left(\frac{1}{n_{eff}}\frac{dn_{eff}}{dT} + \frac{1}{\Lambda}\frac{d}{dT}\right)\Delta T = \lambda_B(\xi + \alpha)\Delta T \tag{11}$$

where α is the thermal expansion coefficient of the fiber (0.55×10^{-6} /°C for fused silica). The quantity ξ represents the thermo-optic coefficient, which is about 8.3×10^{-6}/°C for Ge-doped silica-core fiber, and ΔT is the applied temperature change. Studies carried out on the stability of FBG at high temperature and radiation dose are described in the next sections.

5.2 Studies on temperature stability of Type-I, Type-IIa and thermally regenerated FBGs

The temperature stability of Type-I and Type-IIa gratings is studied using a home-made PID controller based oven which can be operated upto 1100 °C [13].

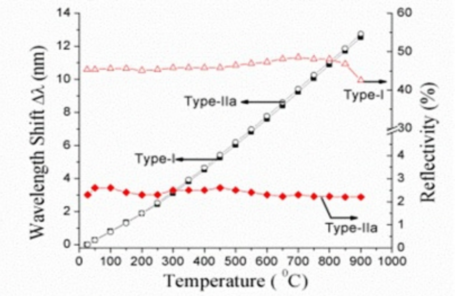

Fig. T.1.9: Variation of reflectivity and shift in λ_B vs temperature.

The Bragg wavelength shift (solid rectangle: Type-I and open circle: Type-IIa) and reflectivity (open triangle: Type I and solid diamond: Type-IIa) of Type-I and Type-IIa FBGs pre-annealed at 800 °C are shown in Figure T.1.9. The average wavelength shift (~13.9 pm/°C) is almost same for both Type-I and Type-IIa FBGs. The reflectivity of Type-I grating is decreased slightly after 800 °C. In contrast for Type-IIa FBG, the reflectivity is almost constant up to 900 °C. Figure T.1.10 shows the variation of λ_B for thermally regenerated FBGs with the change in the temperature. It is observed that after 400 °C, the Bragg wavelength shift is higher. From the Bragg wavelength shift, the temperature can be estimated as [20]:

$$T = T_0 + \frac{a_1}{2a_2}\left[\sqrt{\left(1+\frac{4a_2}{a_1^2}\Delta\lambda\right)}-1\right] \qquad (12)$$

For SM-1500 fiber at T_0 = 31°C, a_1 = 9.60741 pm/°C, $a_2 = 7.84\times10^{-3}$ pm/(°C)^2.

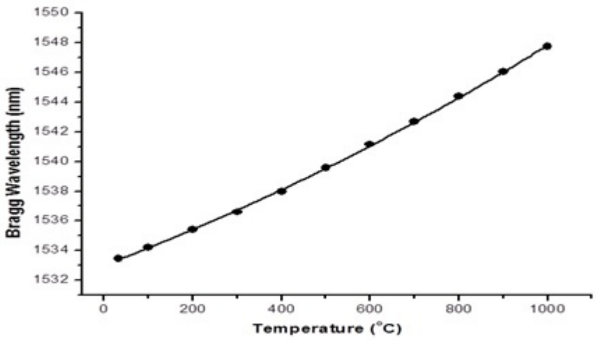

Fig. T.1.10: Bragg wavelength vs temperature.

5.3 Studies on the effect of gamma radiation on FBGs

The effect of gamma radiation on the performance of Type-I (FBG1), negative-index gratings such as Type-IIa (FBG 2) and thermally regenerated FBG (FBG3) are studied upto cumulative radiation dose of 1 MGy [21]. Type-I and Type-IIa FBGs were encapsulated in a stainless steel tube and pre-annealed at 500 °C to eliminate the unstable part of refractive index change.

Figure T.1.11 shows the typical reflection spectra of all FBGs before and after irradiation. It is clear that for all FBGs there is redshift of Bragg wavelength and reduction in bandwidth due to gamma irradiation.

5.4. Application of FBG temperature sensor

5.4.1 Deployment of FBG temperature sensor in Nuclear Fuel Cycle Facilities

The end application here demands sustainability of sensors in high temperature, high EMI and high radiation environment. The sensor for this application is developed using thermally regenerated grating. The FBG was encapsulated in a ceramic tube of length 40 cm, outer diameter 4 mm and inner diameter 1 mm. The top end of ceramic tube was open to insert the FBG while bottom end of ceramic tube was closed. For regeneration, the packaged FBG was heated upto 900 °C in a ramp annealing schedule. The radiation hardness of the packaged thermally regenerated FBG sensor was tested in high radiation environment upto 1 MGy. Bragg wavelength shift of ~ 35 pm was observed after 1 MGy accumulated gamma radiation dose.

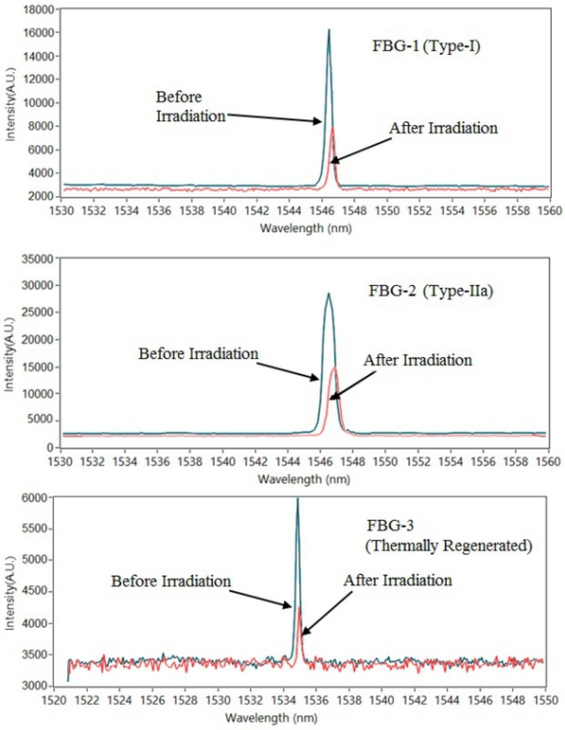

Fig. T.1.11:Interrogator traces of all FBGs (before and after irradiation).

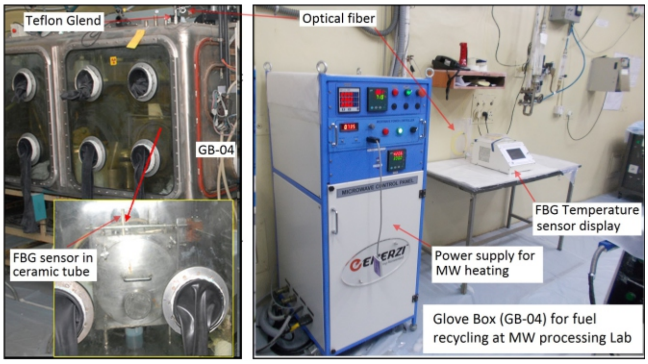

Fig. T.1.12: Deployed temperature sensor at FF, BARC.

Finally, the developed and characterized FBG temperature sensor was deployed at Fuel Fabrication (FF), BARC, Tarapur, to monitor the temperature of microwave (MW) heated nuclear fuel processing chamber as shown in Figure T.1.12 [22]. The maximum temperature of the process chamber was recorded with FBG sensor about 650 °C with an accuracy of ± 1°C.

5.4.2 Deployment of FBG temperature sensor at storage vault of SSSF, NRB, BARC, Tarapur

The FBG based temperature sensor is developed and deployed for monitoring of surface temperature of canisters containing vitrified waste product (VWP), placed in storage vault of SSSF, NRB, BARC, Tarapur.

The storage vault is located below ground level and the canisters placed there contain highly active radioactive waste immobilized in borosilicate glass matrix. Figure T.1.13 shows the FBG sensor connected with normal telecommunication fiber and encapsulated in stainless steel (SS) tube of suitable length to reach the VWP-canister placed in storage vault, and annealed upto temperature of 200 °C. Figure T.1.13(b) shows the variation of online temperature of storage vault from September 4–November 3, 2017 (2 months). The FBG sensor is placed along with the thermocouple. The temperature of storage vault varied from 37 °C to 43 °C.

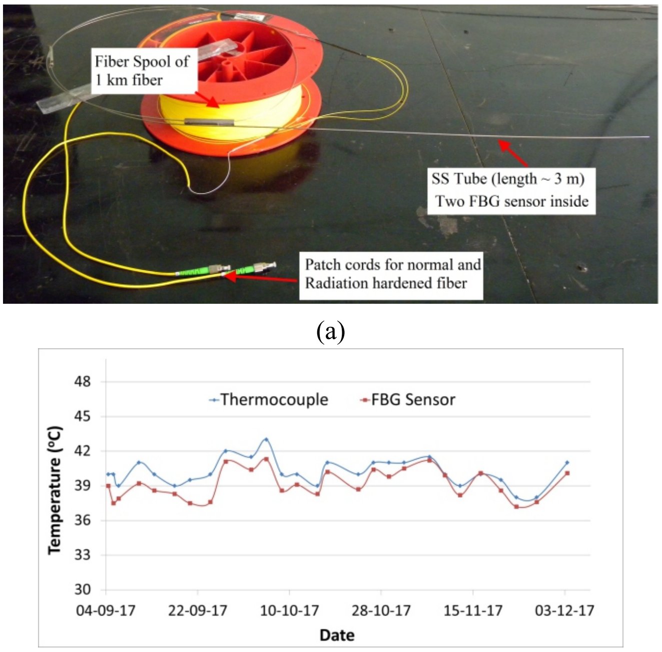

(a)

(b)

Fig. T.1.13: (a) Deployed FBG sensor and (b) variation of canisters surface temperature at SSSF (bottom).

5.4.3 Multipoint temperature monitoring of CuBr laser tube in high-voltage and high-EMI environment

The CuBr laser operating conditions, such as high-repetition rate and high-specific power, demand high-electrical power loading. The high-electrical power loading is a source of high-electromagnetic noise both at the power supply and laser head. FBG based multipoint temperature sensor is fabricated and implemented for this purpose [23]. The maximum operating temperature of the CuBr laser tube reached about 500 °C. Considering a measurement range from room temperature (30 °C) to 500 °C and average sensitivity of the FBG ~13.2 pm/°C, the maximum wavelength shift would be ~ 6.2 nm. Total wavelength span available for sensing in the broadband amplified spontaneous emission (ASE) source is ~40 nm (1525 to 1565 nm). Then the number of distributed point sensors that can be accommodated over a single fiber will be:

$$N=\frac{\lambda_2-\lambda_1}{\left(\left\langle\frac{d\lambda}{dT}\right\rangle\right)(T_2-T_1)}\approx\frac{40}{6.2}\approx 6 \qquad (13)$$

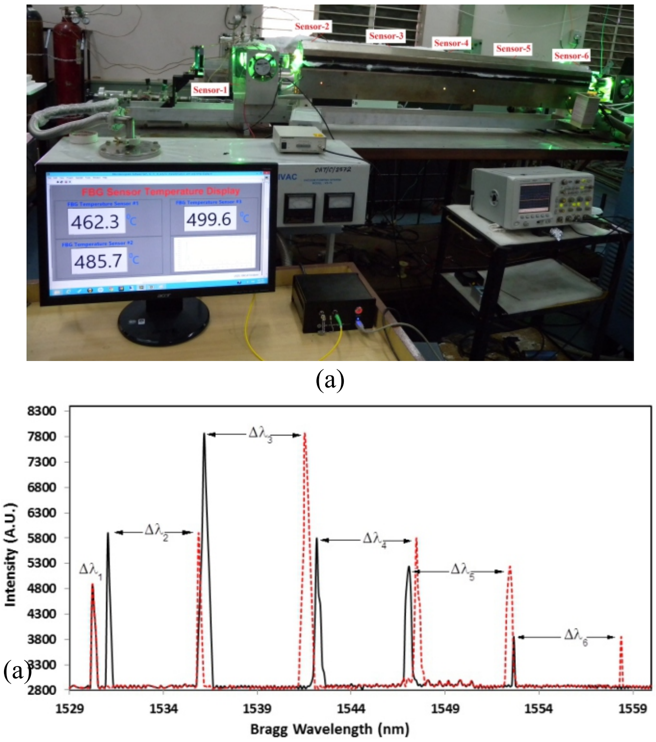

(a)

(a)

(b)

Fig. T.1.14: (a) Multiple FBGs at different locations along the laser tube. (b)Shift in the Bragg peak of FBGs.

Six FBGs at discrete wave length were written. Out of six FBGs, five FBGs (from FBG-2 to FBG-6) are placed along the laser tube as shown in Figure T.1.14(a). Figure T.1.14(b) shows the typical reflection spectrum of the FBG array at the maximum operating input power of 4.3 kW. The Bragg peaks for FBG-2 to FBG-6 are shifted due to the change in the temperature of the laser tube. However, no shift in peak of FBG-1 is observed because of constant ambient temperature. The λ_B shifted from 1531.031 to 1536.670 nm, 1536.954 to 1542.734 nm, 1542.947 to 1549.037 nm, 1549.464 to 1555.654 nm, and 1555.811 to 1562.041 nm for FBG-2, FBG-3, FBG-4, FBG-5, and FBG-6, respectively. The estimated temperature at these points from value of wavelength shift of these FBGs, was 30 °C, 467 °C, 478 °C, 498.5 °C, 499 °C, and 499.5 °C, respectively.

5.4.4 Distributed temperature monitoring of vacuum chamber of dipole magnet DP-12 of Indus-2

The Indus-2 ring at RRCAT is operating at 2.5 GeV and 200 mA. The power deposition due to synchrotron radiation on the wall of vacuum chamber is very intense due to high energy. This in turn leads to instantaneous localized heating of chamber material and may lead to opening of brazing joints of the vacuum components. A twenty point FBG based temperature measurement system is developed and deployed for temperature monitoring of vacuum chamber of bending magnet (DP-12) in Indus-2. The schematic of the distributed temperature sensor is shown in Figure T.1.15. An array of twenty FBGs with different Bragg wavelength in a single fiber is inscribed at the spatial separation of 13 cm, by tilting the phase mask with respect to the fiber as discussed in section

4.5 [17, 23]. The 20 FBGs at spatial separation of ~13 cm and spectral separation of ~1.4 nm, were written. This FBG sensor set-up is annealed at 150 °C before installation. The temperature varied from 18 °C to 35 °C during the operation of Indus-2. The temperature is displayed online on the computer screen using in-house developed software.

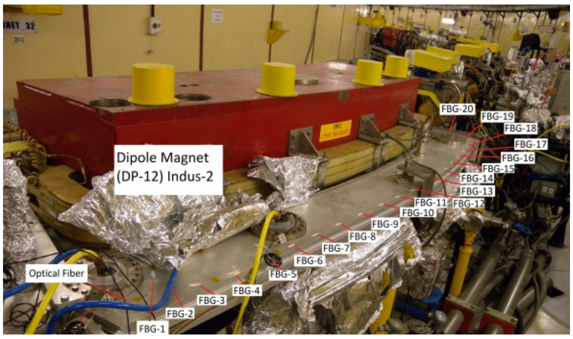

Fig. T.1.15: Twenty point FBG temperature monitoring set-up installed at DP-12.

5.4.5 Development of prototype FBG sensor for coolant channel temperature monitoring of Kakarapar Atomic Power Station 1

A prototype FBG based distributed temperature sensor is developed for temperature monitoring of coolant channel in the high radiation environment of a reactor. The temperature of the coolant channel varies from room temperature (~27 ºC) to 300 ºC. Total available wavelength span for the sensor development was 1525 nm to 1565 nm i.e. 40 nm accordingly total 9 sensors were accommodated in a single fiber, without spectral overlapping with each other. Type-I gratings at nine different Bragg wavelengths were fabricated in a single fiber. The fabricated sensors are packaged in SS tubes after removing their acrylic coating to avoid any unwanted strain in the sensor system. The packaged FBG sensors were heated upto 500 ºC to remove the unstable component of refractive index modulation.

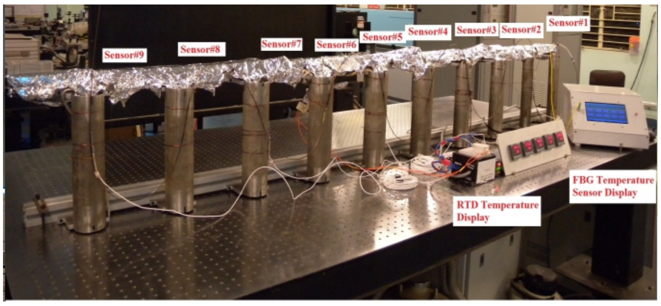

Fig. T.1.16: FBGs encapsulated in SS tube installed on the mock test setup in lab.

A mock test set-up comprising nine tubes as per the geometry of coolant channels of Kakrapar Atomic Power Station 1 (KAPS) was developed as shown in Figure T.1.16. These tubes were placed at a spatial separation ~ 27.5 cm. FBGs were placed on the surface of the tube. RTD based temperature sensors were also placed at for alternative tubes to cross verify the results obtained with FBG sensor. The temperature data was recorded and logged by in-house developed software.

5.5 Application of FBG strain sensor

The shift of the Bragg wavelength could be also written as a function of the strain knowing the material properties of the FBG [19]:

$$\lambda_B = 2n\Lambda_g\left[1-P_e\right]\Delta\varepsilon, \tag{14}$$

where $P_e = \frac{n_{eff}^2}{2}\left[P_{12} - \nu\left(P_{11}+P_{12}\right)\right]$, P_e being the strain optic coefficient, Λ_g = grating spacing, $\Delta\varepsilon$ = change in the applied strain, P_{11} & P_{12} = the stress optic coefficient, ν= Poisson's ratio, n_{eff} = the effective index of the core. So, the Bragg wavelength changes with the applied strain to FBG. For a typical germanosilicate optical fiber: P_{11} = 0.113, P_{12}= 0.252, ν= 0.16 and n_{eff} =1.482. This gives a strain-optic constant of 0.22 for germanosilicate fiber [19].The strain sensitivity of ~ 1.02 pm/με is obtained for Ge-B co-doped fiber.

5.5.1 Development of wheel impact load detection system for railway safety

Study on feasibility of utilizing FBGs developed in RRCAT was carried out for the development of wheel impact load detection (WILD) system for railway safety. This study is carried out by Lab-2-Market (a start-up of Indian Institute of Science, Bengaluru). For measuring the load on the rails, FBG strain sensor was mounted on the web in the inter-sleeper region for vertical load as shown in Figure T.1.17(a).

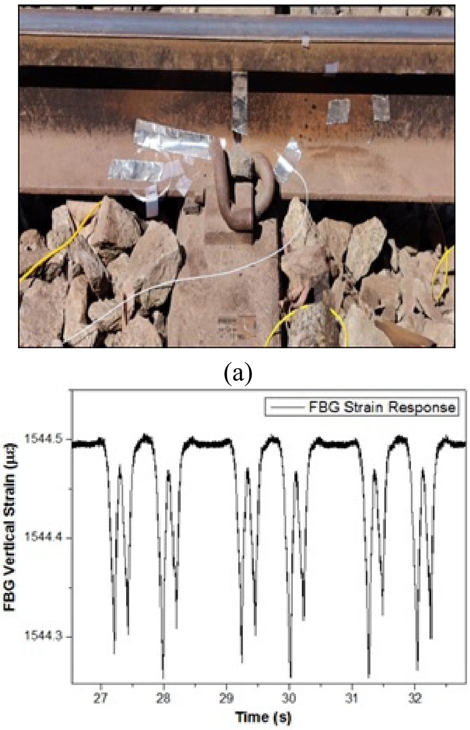

(a)

(b)

Fig. T.1.17: (a) Bare FBG attached to rail. (b) Strain response for 3 coaches with no defective wheels.

The strain response of a normal train, without any irregularities, on the vertically mounted FBG strain sensor is shown in Figure T.1.17(b). The pairs of down-pointing dips correspond to the two pairs of wheels of a bogie. The observed strain data on strain sensor appeared to be clean without any out of the order spikes. Now the strain was measured with flat wheel of 22 mm and 50 mm,respectively. The flats on the wheels were artificially made as shown in Figure T.1.18 and were aligned to hit the rail.


(a) (b)

Fig. T.1.18: Wheel flats of (a) 22mm (b) 50 mm.

Figure T.1.19 shows the strain response of the FBG sensors with wheel flat of 20 mm and 50 mm, respectively. Two sets of 3 peaks corresponds to six wheels of the engine will have higher strain compared to the rest of the wheels. Since the weight of engine is higher than the bogie, the strain imparted by the engine wheels is more compared to the strain imparted by the bogie wheels. Two out of order spikes were clearly visible in the data corresponds to the 22 cm and 50 cm wheel flat. Strain measured on the rail can be correlated to wheel flat.

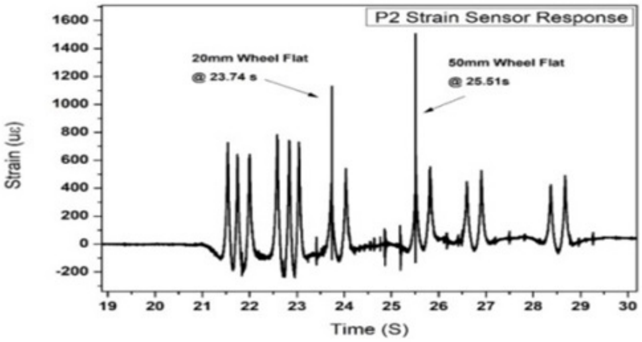

Fig. T.1.19: Strain sensor response with the flat wheel.

5.6 Application of FBG as refractive index sensor

In FBG, the light coupling takes place between well-bound core modes and hence it is intrinsically insensitive to surrounding refractive index (SRI). However, if cladding diameter is reduced partially or totally along the grating region, the effective refractive index is significantly affected by the surrounding medium [24,25]. The wave length shift $\Delta\lambda_B$ is linearly related to changes Δn_{eff} of the effective index n_{eff} of the guided core mode as given by [25]:

$$\frac{\Delta n_{eff}}{n_{eff}} = \frac{\Delta\lambda_B}{\lambda_B} \tag{15}$$

The relations $\Delta\lambda_B\,(n_A)$ and $\Delta n_{eff}\,(n_A)$ are the sensor characteristics of the refractometer.

5.6.1 Studies on the HF based clad etching of FBG

The experimental set-up for HF based etching and chemical sensing is mentioned in [26]. Figure T.1.20(a) shows the variation of λ_{Bragg}, with the etching time at constant temperature of ~25°C. From Figure T.1.20(a), it was noticed that the Bragg wavelength changes about $\Delta\lambda_{Bragg}$ ~ 1.12 nm within 65 minutes.

The etching rate depends on the type of gratings and also on annealing history of grating [27]. The diameter of the etched FBGs is measured by optical microscope (Leica DMC 2900). Figure T.1.20(b) shows the images of the fibers at 50X magnification for the etched FBGs and their intensity variation across the diameter. The measured diameter of the etched FBG is about ~13 μm.

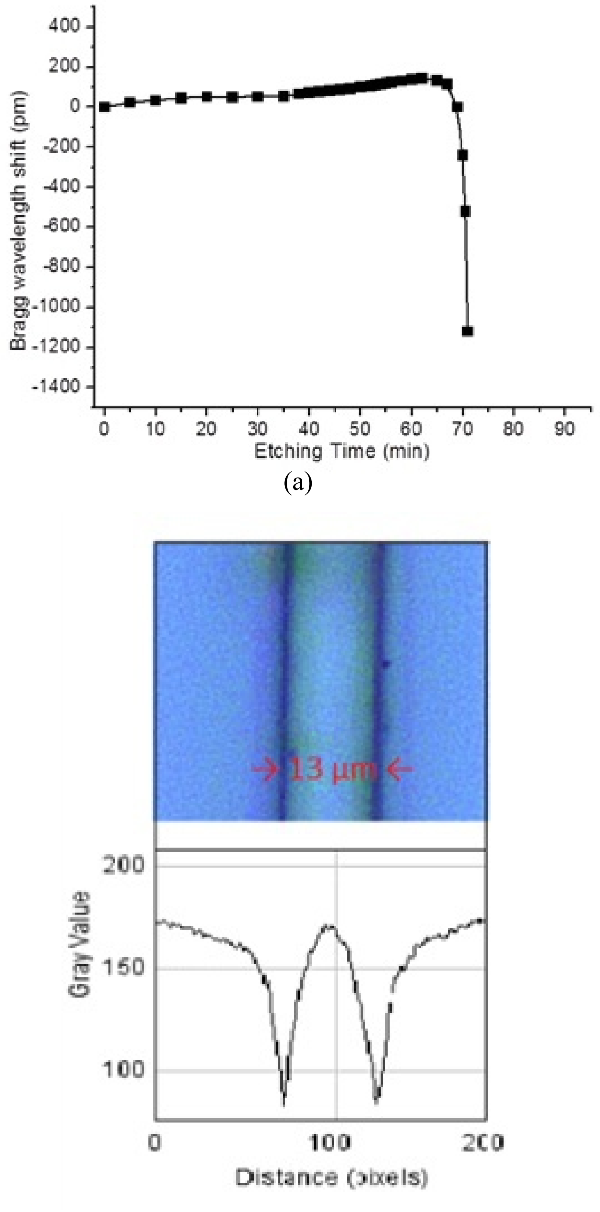

(a)
(b)

Fig. T.1.20: (a) Bragg wavelength shift during HF etching of FBG. (b) Microscopic image of the etched FBG and its intensity profile.

5.6.2 Ethanol detection in petrol

The ethanol proportion in commercially available petrol was monitored using etched FBGs. Figure T.1.21 shows the spectral shift of Bragg peak with different ethanol percentage [28]. As the concentration of ethanol is increased, the peak shows blue shift. It is also noted that the sensor shows higher peak shift per percent change in ethanol proportion in range of 0 – 10 %. It is evident from the figure that a minimum ethanol concentration of 5 % can be detected.

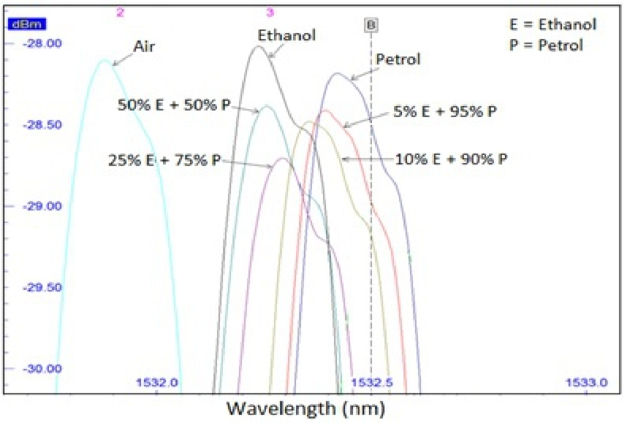

Fig. T.1.21: EFBG reflection spectrum for various ethanol content (%) in petrol.

5.6.3 Determination of methanol content in ethanol

Methanol is very toxic for humans especially when inadvertently got mixed with ethanol. An etched fiber Bragg grating (EFBG) based sensor is developed to perform in-situ measurement of methanol content in ethanol [29]. The estimated refractive index varied from 1.3417 to 1.3386 as the methanol concentration changed from 0 to 10%. Figure T.1.22 shows the Bragg wavelength shifted from 1523.086 nm to 1523.016 nm as the methanol concentration is changed from 0 % to 10 %. The sensitivity of this EFBG is also shown in FigureT.1.22. It shows that the sensitivity of this chemical sensor is almost constant in the range of 6.3 pm to 7 pm per % methanol content in alcohol. The sensitivity of the developed sensor in terms of refractive index unit (RIU) is about 30 nm/RIU. The minimum change in refractive index that can be measured is 2×10^{-4}.

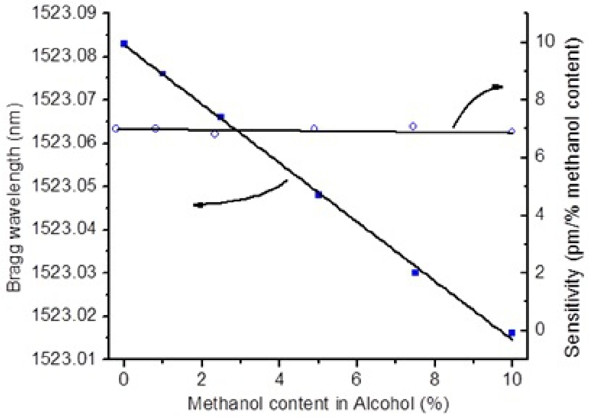

Fig. T.1.22: Bragg wavelength shift and sensitivity of EFBG for methanol content in alcohol for 0% to 10%.

5.6.4 Refractive index sensitivity enhancement using graphene oxide coated etched FBG

A small portion of the cladding of the fiber around FBG is removed and coated by graphene oxide (GO), a single layered material made up of oxidize graphite [28]. Figure T.1.23 shows the change in reflection amplitude with change in ethanol percentage in petrol. From this figure, it is clearly evident that 0.5% ethanol can be easily detected using GO coated EFBG sensor, whereas normal etched FBG based on wavelength shift measurement only detected a minimum of 5% (Figure T.1.21). An etched FBG coated with gold nano-shell particles has shown high refractive index sensitivity for the SRI [30].

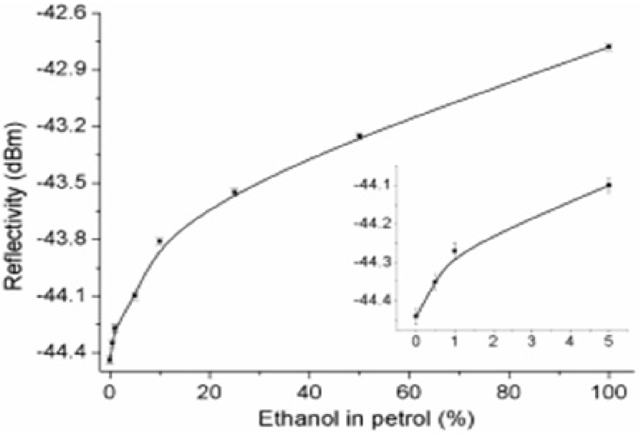

Fig. T.1.23: Change in amplitude with ethanol percentage in petrol.

5.6.5 Refractive index sensitivity of etched thermally regenerated FBG

HF etching of regenerated grating shows unusual behavior compared to that of Type-I gratings [27]. Bragg wave length shift for regenerated grating was $\Delta\lambda_B < 5$ pm. Figure T.1.24 shows the Bragg reflected peak for air (n ~1), methanol (n~1.3194), ethanol (n~1.3417) and ethylene glycol (n~1.4219).

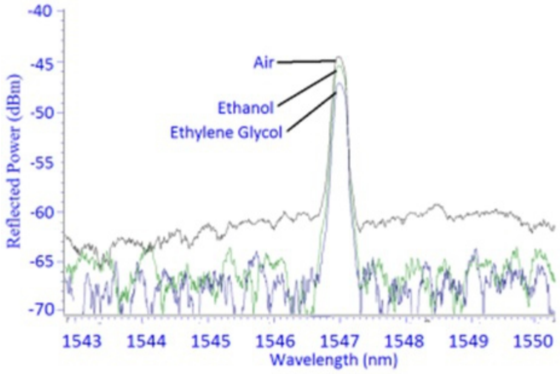

Fig. T.1.24: Variation of reflected power of etched FBG with the surrounding refractive index.

As clear from Figure T.1.24, the shift in Bragg wavelength λ_B= 1546.972 nm is almost insensitive to the surrounding medium refractive index. However, the reflected power is Rp = -44.7 dBm, -45.06 dBm, -45.56 dBm and -47.61 dBm for air, methanol, ethanol and ethylene glycol, respectively. Thus using thermally regenerated HF etched FBG, where no change in wave length occurs with different surrounding media, an intensity dependent sensor can be made to measure to refractive index sensor.

6. Conclusion

In conclusion, technology for inscription of different types of FBGs such as Type-I, Type-IIa, tilted and thermally regenerated, is developed. The in-house fabricated FBGs were applied for the development of temperature, strain, and refractive index sensor. The sensor developed using RRCAT fabricated FBGs have been successfully deployed in nuclear radiation environment and in the development of railway safety equipment. Using etched thermally regenerated FBGs, only intensity dependent refractive index sensor can be developed. The FBG based sensors, due to their multiplexing capabilities, high immunity to extreme environment, compact topology, all optical integration on internet platform, offers wide possibilities for deployment in measurement of multiple parameters in difficult and critical situations.

Acknowledgement

Authors wish to acknowledge the support from Shri S. Kumar, Shri U. Kumbhkar and Shri V. K. Srivastava. The power supply and instrumentation support from Shri Jagdish Kumar and Shri P. K. Agrawal is duly acknowledged. Authors are thankful to Shri R. B. Bhatt and Dr. Gitender Singh, FF (INRP-O), BARC, Tarapur, for installation of FBG sensors at fuel recycling chamber.

References

[1] P. Ferdinand, S. Magne, S. Rougeault, P. Bernage, M. Douay, E. Fertein, F. Lahoreau, P. Niay, J. Bayon, T. Georges, and M. Monerie, Proc. SPIE, vol. 2425, pp. 11–20, Dec. 1994.
[2] F. Berghmans, O. Deparis, S. Coenen, M. Decreton, P. Jucker, NATO ASI Series (Series E: Applied Sciences), Springer, Dordrecht, vol. 285, pp. 131-156, 1995.
[3] A. F. Fernandez, F. Berghmans, B. Brichard, P. Borgermans, A. I. Gusarov, M. V. Uffelen, P. Mégret, M. Decréton, M. Blondel, A. Delchambre, IEEE Trans. Nuc. Sci., 48, 1708-1712, 2001.
[4] A. G. Leal-Junior, C. Marques, A. Frizera, M. J. Pontes, Opt. Fib. Tech., vol. 40, pp. 82– 92, Jan. 2018.
[5] B. Culshaw, J. Dakin, Optical Fiber Sensors System and Applications, Vol 2, Artech House (1989).
[6] R. Kashyap, Fiber Bragg Gratings, Academic Press, New York, 2012.
[7] O. Prakash, R. Mahakud, S.K. Dixit, U. Nundy, Opt. Comm., 263 (1), 65-70 (2006).
[8] O. Prakash, R. Mahakud, S. K. Dixit, Opt. Engg., 50 (11), 114201 (2011).
[9] O. Prakash, S. K. Dixit, R. Bhatnagar, IEEE J. Quant. Electron., 38 (6), 603-613 (2002).
[10] O. Prakash, R. Mahakud, R. Biswal, S. Gurram, H. S. Vora, S. K. Dixit, Appl. Opt., 46, 6210-6217, 2007
[11] R. Mahakud., J. Kumar, O. Prakash, S. K. Dixit, S. V. Nakhe, Appl. Phys. B: Laser and Optics, 121, 283-295 (2015).
[12] A. Othonos and K. Kalli, Fiber Bragg Gratings: Fundamentals and Applications in Telecommunications and Sensing, Artech House, Norwood, Mass. (1999).
[13] O. Prakash, J. Kumar, R. Mahakud, S. K. Agrawal, S. K. Dixit, S. V. Nakhe, IEEE Photon. Techno. Lett., 26, 93-95, (2014).
[14] J. Kumar, O. Prakash, R. Mahakud, S. K. Agrawal, S. K. Dixit, S. V. Nakhe, Opt. Engg., 53, 1171031-6, (2014).
[15] J. Canning, Measurement, 79, 236–249, 2016.
[16] J. Kumar, O. Prakash, R. Mahakud, S. K. Agrawal, A. Mokhariwale, S. K. Dixit, S. V. Nakhe, IEEE Xplore, WRAP2015, no. 1570213269, 1-4, 2017.
[17] O. Prakash, J. Kumar, R. Mahakud, U. Kumbhakar, S. V. Nakhe, S. K. Dixit, PRAMANA, J. Phys., 82, 255-258 (2014).
[18] R. Mahakud, O. Prakash, J. Kumar, S. V. Nakhe, S. K. Dixit, Opt. Commun., 285, 24, 5351-5358 (2012).
[19] A. D. Kersey, M. A. Davis, H. J. Patrick, M. LeBlanc, K. P. Koo, C. G. Askins, M. A. Putnam, E. J. Friebele, J. Light. Wave Technol., 15, 1442-1463, 1997.
[20] R. Mahakud, J. Kumar, O. Prakash, S. K. Dixit, Appl. Opt., 52, 7570-7579, 2013.
[21] J. Kumar, O. Prakash, S. Kumar, S. K. Dixit, Y. K. Bhardwaj, S. V. Nakhe, Opt. Engg., 58, 057108, 2019.
[22] J. Kumar, G. Singh, M. K. Saxena, O. Prakash, S. K. Dixit, S. V. Nakhe, IEEE Sensors Journal, 21, 7613-7619 (2021).
[23] J. Kumar, O. Prakash, S. K. Agrawal, R. Mahakud, A. Mokhariwale, S. K. Dixit, S. V. Nakhe, Opt. Engg. (Letters), 55, 090502-1 to 4, 2016.
[24] A. Iadicicco, A. Cusano, S. Campopiano, A. Cutolo, M. Giordano, “Thinned fiber Bragg gratings as refractive index sensors”,” IEEE Sensors Journal, 5, 1288-1295 (2005).
[25] K. Schroeder, W. Ecke, R. Mueller, R. Willsch, A. Andreev, Meas. Sci. Tech. 12 (7), 757-764 (2001).
[26] J. Kumar, R. Mahakud, O. Prakash, S. K. Dixit, Opt. Engg., 52, 0544021-26 (2013).
[27] J. Kumar, O. Prakash, R. Mahakud, S. K. Agrawal, S. K. Dixit, S. V. Nakhe, J. Canning, Sensors and Actuators B: Chemical, 244, 54-60 (2017).
[28] P. Kumar, S. Kumar, J. Kumar, G. S. Purbia, O. Prakash, S. K. Dixit, Meas. Sci. Tech., 31, 2,025109 (2020).
[29] J. Kumar, R. Mahakud, U. Kumbhakar, O. Prakash, S. K. Dixit, S. V. Nakhe, Optik- International J. Light and Electron Optics, 126, 5698-5702 (2015).
[30] J. Burgmeier, A. Feizpour, W. Schade, B. M. Reinhard, Opt. Lett., 40, 546-549 (2015).